Available online at www.sciencedirect.com

SciVerse ScienceDirect

Ceramics International 39 (2013) 4089–4098

CERAMICS INTERNATIONAL

www.elsevier.com/locate/ceramint

Hydrothermal synthesis and luminescence properties of YF_3:Ln (Ln=Sm, Dy, Tb and Pr) nano-/microcrystals

Feng Tao[a,b,*], Congrong Hu[a], Zhijun Wang[a,b], Geng Zhu[a], Yufeng Sun[a,b], Da Shu[a]

[a]College of Mechanical and Automotive Engineering, Anhui Polytechnic University, Wuhu, Anhui 241000, PR China
[b]Anhui Provincial Laboratory of High Performance Nonferrous Metals Material, Wuhu, Anhui 241000, PR China

Received 24 September 2012; received in revised form 28 October 2012; accepted 30 October 2012
Available online 5 November 2012

Abstract

YF_3:Ln (Ln=Sm, Dy, Tb and Pr) nano-/microcrystals with uniform morphology and size have been successfully prepared by a facile, and environmentally friendly hydrothermal method. X-ray diffraction (XRD), field emission scanning electron microscopy (FE-SEM), transmission electron microscopy (TEM), high-resolution transmission electron microscopy (HRTEM), and selected area electron diffraction (SAED) have been used to study the morphologies and crystal structure of the products. The effects of the molar ratio of EDTA to Y^{3+}, and chelator on the crystal growth have been investigated in detail. The time-dependent experiments have been conducted to investigate the morphology evolution process. Based on the results, a possible growth mechanism is proposed. The photoluminescence spectra at room temperature show that the as-prepared YF_3:Ln (Ln=Sm, Pr, Tb and Dy) nano-/microcrystals show strong light emissions with different colors coming from different activator ions. It is noticed that morphology and size of the products have great influence on their emission intensity. Interestingly, in the YF_3:Sm system, we observed the Sm^{2+} emission peaks when excited at 323 nm. The results reveal that some of the Sm^{3+} ions should have been reduced to the divalent state during the hydrothermal process.
© 2012 Elsevier Ltd and Techna Group S.r.l. All rights reserved.

Keywords: A. Powders: chemical preparation; B. Nanocomposites; C. Optical properties; YF3

1. Introduction

Lanthanide ions play an important role in modern technology for its superior luminescent properties [1–6]. The color of the emitted light depends on the lanthanide ion. For instance, Sm^{3+}, Dy^{3+} and Tb^{3+} emit orange, blue and green light, while Pr^{3+} ion can emit different colored light depending on the host lattice [7]. Luminescence from lanthanide-doped materials have recently drawn considerable attention because of their potential applications in display devices, optical communication, solid-state lasers, catalysis, and biological labeling [1,2,8,9]. For example, $InBO_3$:Tb^{3+} is a candidate for application in projection cathode-ray tubes [10], $SrAl_2O_4$:Dy^{3+}, Eu^{2+} has been regarded as a useful green phosphor of the long persistent phosphorescence [11]. The $LaInO_3$:Re^{3+} (Tb, Pr, Sm) phosphors have potential application in field emission display devices [12]. Such application relies on the luminescence of lanthanide with sharp lines, high photochemical stability and long fluorescence lifetime. In addition, their structures, shapes, and sizes also have great effect on their luminescence properties, such as tunable wavelengths, rapid responses, and high efficiencies. Thus the controlled synthesis of these new nanomaterials has sparked considerable interest.

In comparison with oxygen-based systems, the fluoride lattices possess very low vibrational energies and therefore minimal quenching of the excited states of the rare earth ions [9] is observed. Yttrium trifluoride (YF_3) is a well-known fluorescent host lattice owing to its wide band gap and low vibrational energies. Till now, YF_3 micro-/nanocrystals with different shapes, including hollow peanut-like structures [13], quadrilateral and hexagonal shape nanoparticles [14], octahedron microcrystals [15], sub-microflowers [16]

*Corresponding author at: College of Mechanical and Automotive Engineering, Anhui Polytechnic University, Wuhu, Anhui 241000, PR China. Tel.: +86 553 2871252.
E-mail address: taozhi@ahpu.edu.cn (F. Tao).

0272-8842/$ - see front matter © 2012 Elsevier Ltd and Techna Group S.r.l. All rights reserved.
http://dx.doi.org/10.1016/j.ceramint.2012.10.263

and polyhedral microcrystals [17], have been investigated extensively. An appreciable amount of reports have been published on the photoluminescence of YF_3 doped different lanthanide ions [18–25]. However, despite great progress that had been realized in this field, the shape-controllable synthesis of high-quality lanthanide-doped fluoride nano-/microcrystals, especially control of the YF_3-based nanophosphors, is still a big challenge, which is important for the exploration of their materials properties and for potential applications.

In this paper, we report the synthesis of YF_3:Ln (Ln = Sm, Pr, Tb and Dy) nano-/microcrystal with tunable morphology and excellent luminescent properties by a facile hydrothermal method. The morphology evolution process was investigated by the time-dependent experiment. The structure, formation process, and their room photoluminescence behaviors were investigated in detail. Furthermore, we discussed the shape-dependent luminescent properties and the energy transfer from Sm^{2+} ions to Sm^{3+} ions in YF_3:Sm nano-/microcrystal.

2. Experimental section

2.1. Synthesis

All reagents were of analytical grade and used without further purification. Yttrium oxide (Y_2O_3, 99.99%), samarium oxide (Sm_2O_3, 99.99%), praseodymium oxide (Pr_2O_3, 99.99%), dysprosium oxide (Dy_2O_3, 99.99%), terbium oxide (Tb_4O_7, 99.99%), ethylenediamine tetraacetic acid disodium salt (Na_2H_2EDTA, AR), ammonium fluoride (NH_4F, AR), and HNO_3 (AR) were purchased from Shanghai Chemical Reagents Company. In a typical procedure, 2 mmol Ln_2O_3 (Ln = Y, Sm, Pr, Dy and Tb) was dissolved in dilute nitric acid (3 mol L^{-1}, 25 mL) completely to form a clear solution and the pH value of the solution was adjusted to about 2–3 with dilute $NH_3 \cdot H_2O$. Then, 0.745 g of Na_2H_2EDTA was added to the solution to form a chelated yttrium complex. After magnetic stirring for 10 min, 0.51 g NH_4F was added into the mixture under vigorous stirring. The resultant suspension was transferred into a 30 mL Teflon-lined autoclave. The Teflon vessel was then filled with distilled water up to about 80% of its volume. After the autoclave was tightly sealed, it was heated at 180 °C for 48 h, and then cooled down to room temperature naturally. The products were washed several times with distilled water and absolute ethanol in turn, and then dried in air at 70 °C for 6 h. Additionally, different hydrothermal treatment times at 180 °C were selected to investigate the morphological evolution process of YF_3:Ln^{3+}.

2.2. Characterization

The phase and composition of the products were determined by a Bruker D8 X-ray diffractometer with Cu Kα radiation ($\lambda = 0.15418$ nm) in the range of $20° \le 2\theta \le 80°$. The morphologies of the samples were observed by transmission electron microscope (TEM, H-800) and a field emission scanning electron microscopy (FESEM, Hitachi S4800). A high-resolution transmission electron microscope (HRTEM, JEOL-2010) and selected area electron diffraction (SAED) techniques were employed to characterize the crystal structure. The photoluminescence spectra were recorded with steady-state/lifetime fluorescence spectrometer (FLUOROLOG-3-TAU) at room temperature.

3. Results and discussion

3.1. Morphology and microstructure of the products

The crystal structures and phase purity of the studied samples were performed by XRD. As shown in Fig. 1, the four samples exhibit the peaks of pure crystalline orthorhombic YF_3 [space group *Pnma* (62)], which are consistent with the literature data (JCPDS no. 74-0911). No peaks of other impurity crystalline phases were detected, which suggested that the completely crystalline and pure-phase Ln^{3+} doped YF_3 could be obtained by using this facile hydrothermal method. Although the diffraction peaks of these samples are in the similar position, the peak intensity is different as the introduction of different dopant changed the YF_3 lattice parameters. The ionic radii of RE^{3+} ($R(Sm^{3+}) = 1.66$ Å, $R(Dy^{3+}) = 1.589$ Å, $R(Tb^{3+}) = 1.592$ Å, $R(Pr^{3+}) = 1.648$ Å) are similar to those of Y^{3+} ($R(Y^{3+}) = 1.62$ Å), so it is assumed that RE^{3+} ion can substitute Y^{3+} by causing little lattice distortion.

The morphologies of the samples were examined using FESEM and TEM. The general morphologies of the as-prepared samples are independent of the doped Ln^{3+} ions in YF_3. The typical FESEM and TEM images of the Sm^{3+}-doped YF_3 products obtained at 180 °C for 48 h are presented in Fig. 2. As can be seen from the low magnification SEM image (Fig. 2a), the as-synthesized sample consists of a large quantity of regular truncated octahedral with uniformity and monodispersity and well-defined crystallographic facets.

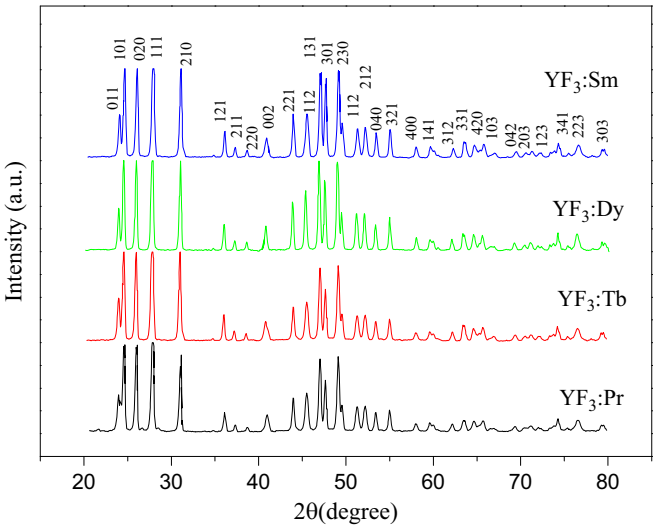

Fig. 1. X-ray diffraction pattern of the as-obtained product.

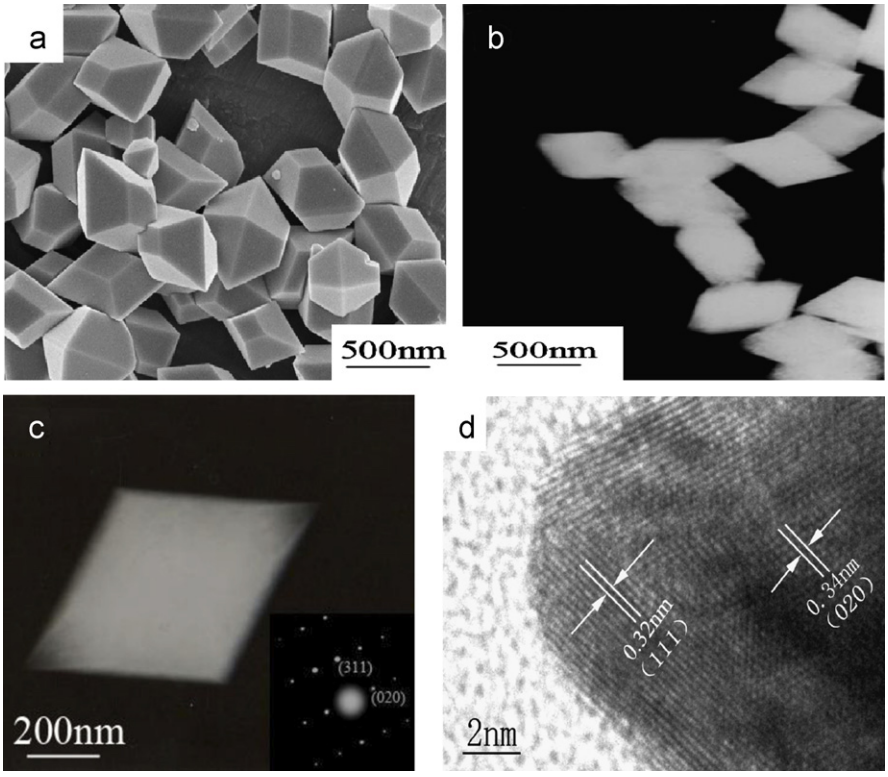

Fig. 2. (a) Typical FESEM image of the YF_3:Sm crystals obtained at 180 °C for 48 h; (b) typical TEM image of YF_3:Sm crystals obtained at 180 °C for 48 h; (c) TEM image of a single YF_3:Sm crystal and ED pattern and (d) HRTEM image of a single YF_3:Sm crystal.

The average length is about 450 nm. It is also noticed in Fig. 2a that some small particles are attached on the surfaces of the octahedra, which suggests these small particles may serve as building blocks for the growth of the nanooctahedra. The TEM image of the sample is shown in Fig. 2b, which shows the length of crystal is 450 nm, in agreement with the SEM results. Fig. 2c shows the TEM images of a single nanooctahedron and selected area electron diffraction (SAED) pattern. The diffraction spots are indexed to the (311) and (020) plane of the orthorhombic YF_3, which shows that the octahedron is a well-developed single crystal. Fig. 3d shows a typical HRTEM image of a relatively small truncated octahedron with a rhombus base. The measured lattice spacing is about 0.32 and 0.34 nm corresponding to the distances of the {111} and {020} planes of the orthorhombic YF_3:Sm, respectively. The HRTEM image also reveals the single-crystal nature of the product.

A series of experiments was carried out to understand the effect of EDTA on the final morphology. Fig. 3 gives the FESEM images of the YF_3:Sm crystals prepared under 180 °C for 48 h with different conditions. It shows that EDTA is indispensable to the morphology and size of the products. In the absence of EDTA, the products are rice-like nanoparticles (Fig. 3a). If the CTAB is used as the chelator instead of EDTA, the products are irregular nanoparticles (Fig. 3b).

The crystal size and shape of the products seem to be independent of the reagent concentrations according to our experiments. When the molar ratios of Ln^{3+}-to-EDTA (2:1) and Ln^{3+}-to-F^- (1:3) are kept unchanged, decreasing or increasing the reagent initial concentrations does not cause the shape and size of crystals to change significantly (Fig. 3c). However, if the molar ratio of Ln^{3+}-to-EDTA is increased to 4:1, the product are spheres with about 25 nm diameter (Fig. 3d). The addition of an appropriate quantity of the chelating agent EDTA may have helped the separation between the nucleation and growth stages, since the two processes lie in different concentration zones. At nuleation stage, when the EDTA concentration is lower (molar ratio of Ln^{3+}/EDTA = 4), the capping of EDTA on the surface of prepared nanoparticles prevents further aggregation. It is reasonable to speculate that the rare-earth ions are located in nucleation than the growth stage due to the presence of the EDTA. As a result, the particle size is small. On the contrary, with an increase in the EDTA concentration (the Ln^{3+}/EDTA ratio is equal to 2), the selective interactions of EDTA with the {010} and {111} crystallographic planes make a significant decrease in the growth rates along {010} and {111} planes. According to Bravais's law, the retained crystal facets are the ones with the slowest growth rates [26]. As a result, the truncated octahedra of YF_3:Sm with abundant trapezoid {111} facets over the rhombic {010} bottom planes are obtained. The result suggests that the appropriate molar ratio of Ln^{3+}/EDTA is crucial for the formation of pure and uniform nanostructure.

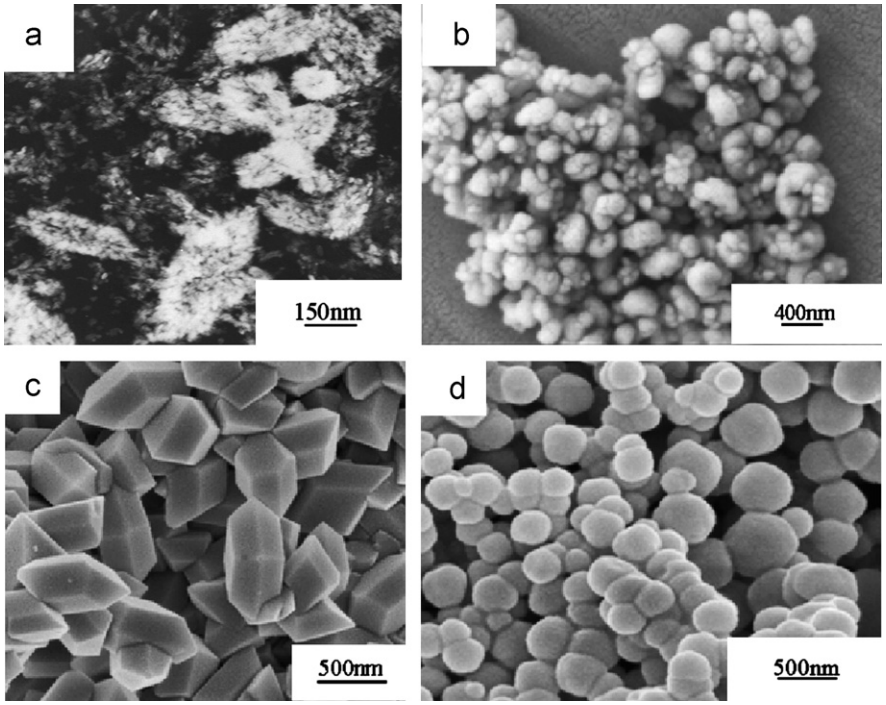

Fig. 3. (a) TEM and (b–d) FESEM images of YF_3:Sm samples obtained under different conditions: (a) without EDTA; (b) with CTAB; (c) $n{Ln^{3+}}=3$ mmol ($n{Ln^{3+}}$-to-nEDTA=2:1, $n{Ln^{3+}}$-to-$n{F^-}=1:3$) and (d) $n{Ln^{3+}}$-to-nEDTA=4:1. All of the samples were hydrothermally treated at 180 °C for 48 h.

To investigate the detailed formation mechanism of YF_3:Sm nanocrystals, time-dependent experiments were conducted keeping the other reaction conditions unchanged. Fig. 4 shows the FESEM image of Ln^{3+} doped YF_3 samples obtained at 180 °C for various reaction periods. At $t=5$ h, the products are all small sphere particles with the diameter about 300–500 nm (Fig. 4a). When $t=10$ h, peanut shape microstructures are obtained (Fig. 4b). By careful observation of Fig. 3b, we can find that the peanut shape microstructures are composed of tens of uniform flake, and these flakes are assembled by nanoparticles. Fig. 4c shows the FESEM image of the products obtained at 15 h. The product is the flower-like nanostructure composed of small irregular polyhedron. When extending the reaction time to 20 h, most of the samples turn to irregular small polyhedron (Fig. 4d). Prolonging time to 48 h, the morphology turns to regular truncated octahedron (Fig. 2a).

In the present work, based on the time-dependent experiments, the schematic illustration for the possible growth process is shown in Fig. 5. The result shows that there exists a competition between these crystals through separation, combination, and re-separation process at different scales [27], and the growth procss of crystals can be divided into space expansion, space occupation and space optimization [28]. When a critical supersaturation of the particle-forming species is reached, YF_3:Ln^{3+} simple sphere nanoparticle (Fig. 5a) firstly formed by Y^{3+} reacts with F^- under the hydrothermal condition. Then, space expansion will occur and sphere nanoparticles will congregate together (Fig. 5b) via oriented attachment to build two-dimensional sheet [29]. The newly formed particle from solution will be adsorbed on the surfaces of the two-dimensional sheet along the space instruction to form the complex peanut shape microstructures (Fig. 5c). With the reaction proceeding, space occupation will begin. Small and more complex flower-like structures (Fig. 5d) will be formed by the diffusion-control growth occurring on the surface. The branch can continue to grow by adsorbing the nutrient element from the surrounding solution. Then space optimization will commence and simpler polyhedron will be formed for the different growth rates of different crystal faces as shown in Fig. 5e. Finally, the preferential adsorption of EDTA on the {010} and {111} crystallographic planes leads to the formation of truncated octahedra (Fig. 5f).

3.2. Optical properties

It is known that the concentration of the doping ions will affect the luminescence properties. Take the YAG:Sm powders for example, when concentration of Sm is over 3 mol%, the emission may weaken due to self-concentration quenching [2]. Fig. 6 displays the room temperature excitation ($\lambda_{em}=599$ nm) and emission ($\lambda_{ex}=399$ nm) spectra of 3 mol% Sm^{3+} doped YF_3 truncated octahedra nano-/microcrystal. The excitation spectrum, recorded from 240 to 560 nm, is composed of several sharp lines corresponding to the characteristic absorption bands for f–f transition in Sm^{3+}. The strongest excitation line at 399 nm corresponds to the $^6H_{5/2}$–$^4F_{7/2}$ transition. Some small and sharp lines can

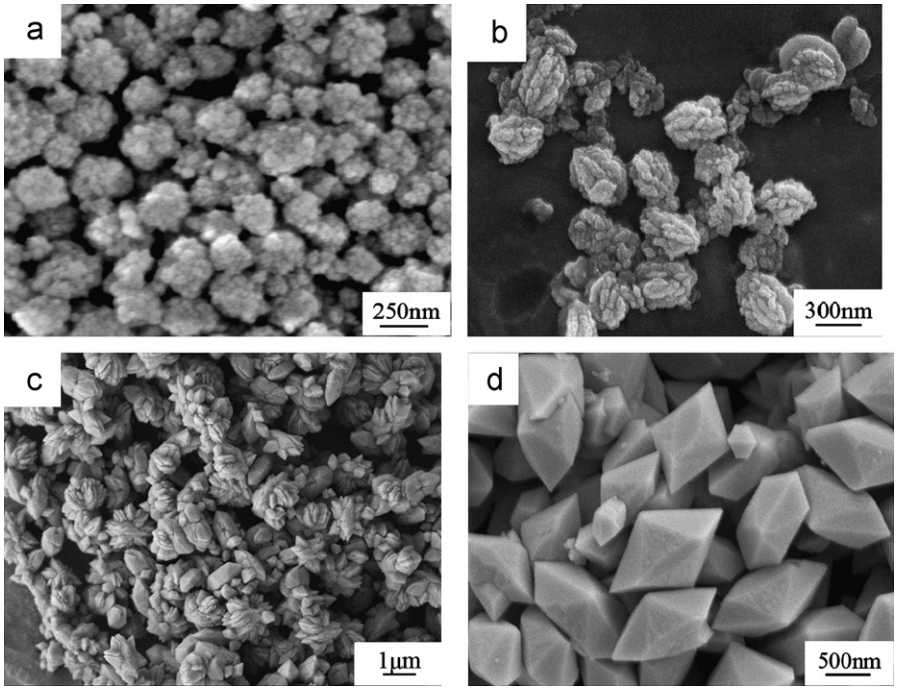

Fig. 4. Typical FESEM images of YF_3:Sm crystals obtained at 180 °C for different reaction times (a) 5 h; (b) 10 h; (c) 15 h and (d) 20 h.

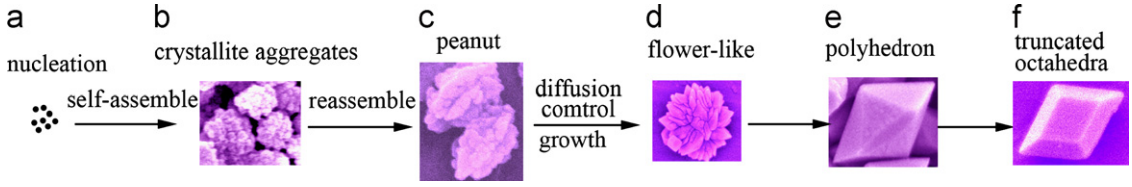

Fig. 5. Schematic diagrams for the growth process based on the time-dependent experiment. (b) 5 h, (c) 10 h; (d) 15 h, (e) 20 h and (f) 48 h.

also be observed in the range of 240–300 nm in the excitation spectrum. The prominent excitation at 399 nm has been selected for the measurement of emission spectrum of YF_3:Sm^{3+}. Three strong emission bands are observed at ~558, ~599, and ~647 nm in the yellow to red region (Fig. 6b), which correspond to a group of typical $^4G_{5/2}$—^6H_J (J=5/2, 7/2, 9/2) transitions of Sm^{3+} and one weak emission band at 699 nm for the transition of $^4G_{5/2}$–$^6H_{11/2}$ for Sm^{3+}. Compared with the previous report [30], the positions of the emission peaks have a slight blue shift which is obviously due to the different crystal field created around Sm^{3+} in each matrix.

Fig. 6c shows the RT emission spectra of the as-prepared YF_3:Sm nanocrystals with different morphologies (the excited wavelength is 399 nm). With the gradient morphology conversion from peanut to truncated octahedral, the emission peak positions have not significantly changed. But the intensity of the peaks is obviously enhanced, which shows that the luminescence intensity of the YF_3:Sm crystal is remarkably influenced by the morphology of the products. The specific surface area is different for a different morphology, which causes the different luminescence centers and surface defects; thus the luminescence intensity is also different. The differences in the morphology, dimension and the crystallization of samples may lead to the change in its local area symmetry, so the ratio of the transition intensity will change. Fig. 6d shows the relationship between the intensity of the 599 nm, 558 nm, 647 nm, 699 nm emission peaks and the morphologies of YF_3:Sm nanocrystals, which shows that luminous intensity of samples depends on its morphology.

In Fig. 6b, we can find a weak emission band centered at about 450 nm (as shown in the asterisks) which do not belong to Sm^{3+}. To identify the origin of this emission, the excitation spectra for emission at 450 nm were studied. It yielded a strong band at 323 nm as shown in Fig. 6e. Emission spectrum for excitation at 323 nm (Fig. 6f) exhibits a strong emission band at 393 nm. The emissions due to Sm^{3+} almost cannot be found clearly indicating that the emissions are due to a species other than Sm^{3+} ions. Interestingly, when excited at 342 nm, the strong emission band and Sm^{3+} characteristic emission peaks co-exist. Fig. 6g shows the emission spectra under different excitation wavelengths, which clearly indicate that the center and the intensity of the broad emission band varied with the changing excitation wavelength. When the excitation wavelength was changed from 323 nm to 399 nm, the broad

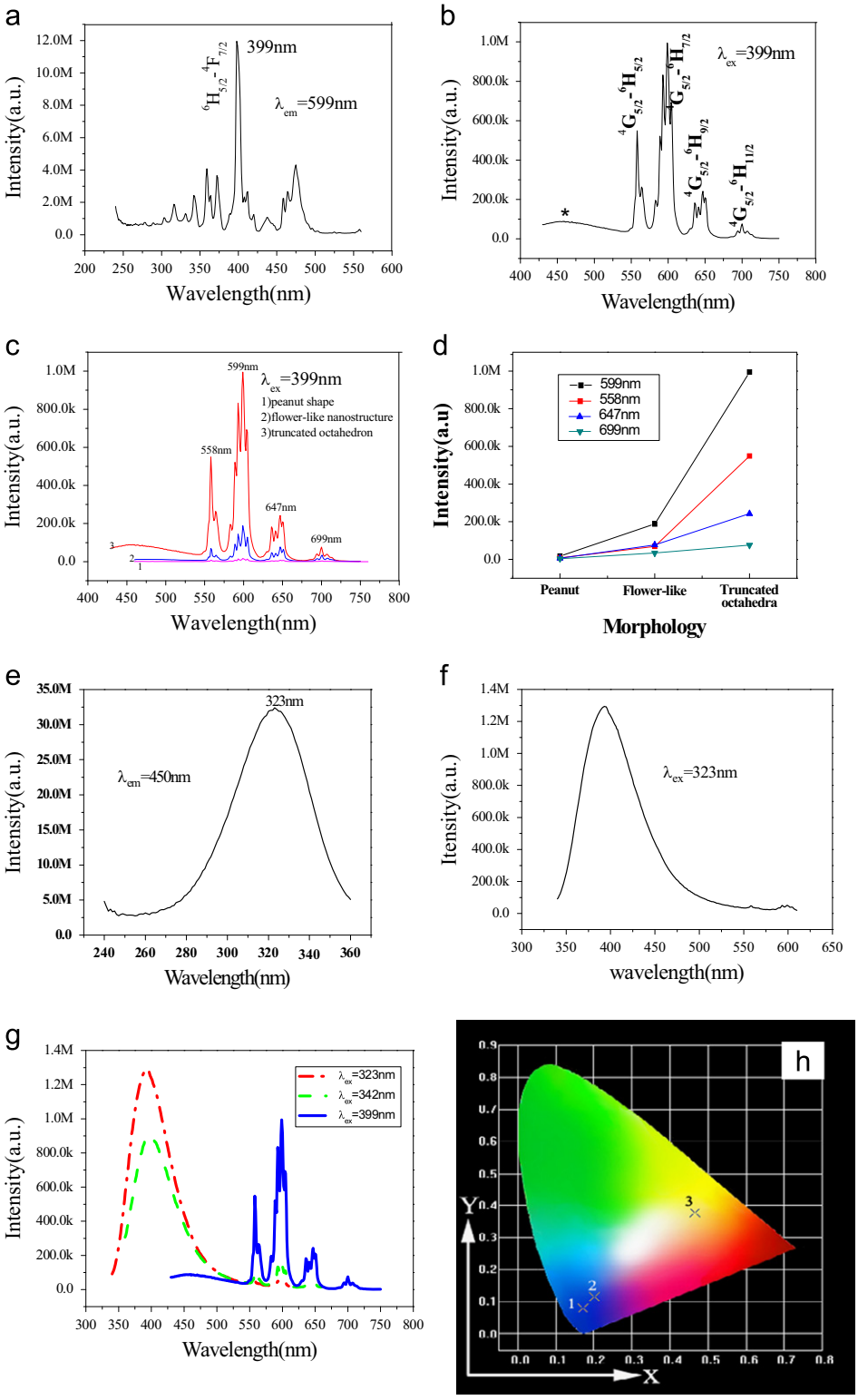

Fig. 6. RT photoluminescence spectra of YF_3: 3 mol% Sm truncated octahedra crystal (EX slits=2 nm, EM slits=5 nm): (a) excitation spectra (λ_{em}=599 nm); (b) emission spectra (λ_{ex}=399 nm); (c) emission spectra of different morphologies (λ_{ex}=399 nm); (d) relationship between the luminescence intensity and the morphology of YF_3:3 mol% Sm microcrystal; (e) excitation spectra (λ_{em}=450 nm); (f) emission spectra (λ_{ex}=323 nm); (g) emission spectra at different excitation wavelengths and (h) the CIE chromaticity diagram for the 0.03 mol% Sm doped YF_3 truncated octahedra micro-/nanocrystal under different excitation wavelengths (1) 323 nm, (2) 342 nm, (3) 399 nm. (For interpretation of the references to color in this figure legend, the reader is referred to the web version of this article.)

emission band center moved from 393 to 450 nm correspondingly, and the intensity is reduced. This phenomenon is very similar to the result reported by us in YF_3:Eu nanocrystal [25]. In that system, some of the Eu^{3+} ions have been reduced to the divalent state in the preparation process, which is inhibited in the presence of EDTA, because of the strong stabilizing

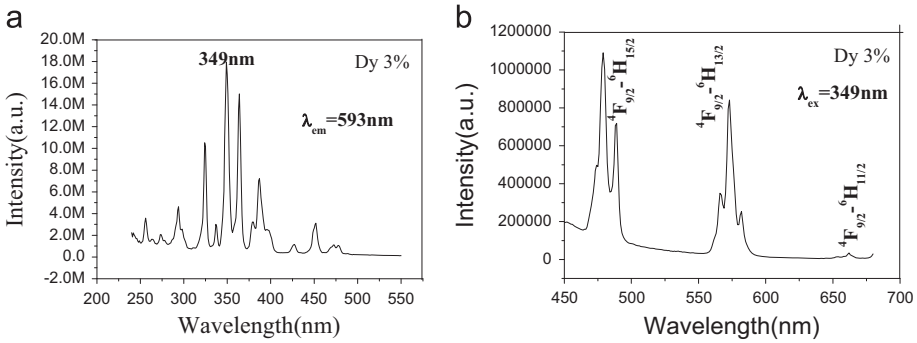

Fig. 7. RT photoluminescence spectra of YF_3:3 mol% Dy^{3+} truncated octahedra micro-/nanocrystal (EX slits=2 nm, EM slits=5 nm): (a) excitation spectra (λ_{em}=593 nm) and (b) emission spectra (λ_{ex}=349 nm).

effect of EDTA on Eu^{3+} [1]. So it is reasonable to deduce that the redox reaction might occur, some of the Sm^{3+} ions are reduced to form Sm^{2+}. The broad-band luminescence is due to interconfigurational $4f^65d \rightarrow 4f^6$ electronic transitions in Sm^{2+} [31]. In contrast to the intraconfigurational f–f transitions, these transitions are parity–allowed and therefore more intense than f–f transitions. Due to the interaction of the 5d-electrons with the ligand ions the bonding strength changes upon 4f–5d excitation, giving broad absorption and emission bands instead of lines [32]. At the 342 nm excitation wavelength, the appearance of both narrow-line f→f and wide-band $4f^65d \rightarrow 4f^6$ luminescence can be related to the co-existence of two kinds of crystallographic sites for Sm (substituting Y^{3+}) in YF_3.

Divalent samarium has been of considerable interest to researchers for several decades. Like europium but unlike other rare-earth ions, samarium is quite stable in the 2+ oxidation state and can be incorporated in this valence state in a larger number of different crystalline hosts [31]. Detailed investigations of the absorption and fluorescence of Sm^{2+} in CaF, SrF, and BaF were carried out by Kaiser and coworkers [33,34]. At even higher energies, usually in the UV and VUV, $4f^6$ to $4f^55d$ transition can be observed. The Sm^{2+} emission in different hosts lies in a characteristically different range due to different structures. Generally, spectra of Sm^{2+} systems display broad bands in spectral range of 250–550 nm corresponding to interconfigurational $4f^55d$–$4f^6$ transition, presenting two split components t_{2g} and e_g of 5d excited state from rare earth ion [35,36]. Under irradiation with visible light, the Sm^{2+} ions are generally excited into the $4f^55d$ continuum. Through coupling with the crystal lattice, the excited ions can give part of their excitation energy to the lattice and land in the 5D levels of the $4f^6$ configuration which generally lie below the $4f^55d$ continuum. From these levels the excited Sm^{2+} ions may return with emission of photons to the various components of the ground multiplet. Moreover, the fact that the pumping transitions are allowed transitions means that even small quantities of Sm^{2+} generate noticeable fluorescence [35].

Fig. 6h shows the CIE chromaticity diagram for 3 mol% Sm doped YF_3 microcrystal under different excitation wavelengths. From Fig. 6h we can find that the emission colors might be further changing the excitation wavelength finely. When the excitation wavelength increased gradually from 323 nm to 399 nm, the emission color changed from blue to orange. For instance, when excited at 323 nm, YF_3:Sm exhibits blue color (CIE chromaticity coordinates x=0.173, y=0.081, point 1 in Fig. 6h), whereas when excited at 399 nm, YF_3:Sm exhibits slight orange color (x=0.466, y=0.377, point 3 in Fig. 6h). That is to say, we can tune the emission color of YF_3:Sm by changing the excitation wavelength. This clearly shows the influence of excitation wavelengths on the emission color, which is of great interest and hence this research is ongoing.

The same procedure was used to study doped YF_3 microstructures with Tb^{3+}, $Dy^{3+}$and Pr^{3+}. Fig. 7 shows the PL excitation and emission spectra of the 3 mol% Dy^{3+} activated YF_3 phosphor. The excitation spectrum monitored at orange emission from Dy^{3+} ion indicates several bands. Dy^{3+} with $4f^9$ configuration has complicated f-block energy levels; therefore various possible transitions between these levels are highly selective, and show sharp line spectra [2,37]. The excitation spectrum in the range of 250–550 nm is due to f→f transition of Dy^{3+} ion having highest intensity peak at 349 nm, which is assigned to $^6H_{15/2} \rightarrow {}^6M_{21/2}$ transition. The emission spectrum for Dy^{3+} ions in YF_3 phosphor gives emission peaks at 478 nm (blue), 573 nm (yellow) and a small peak at 670 nm (red). The transitions involved in blue, yellow and red bands of Dy^{3+} ion are well known. These bands have been identified as $^4F_{9/2} \rightarrow {}^6H_{15/2}$, $^6H_{13/2}$, $^6H_{11/2}$ transitions [3,22]. The CIE coordinates for the emission spectrum of YF_3:3 mol% Dy^{3+} are determined as x=0.260, y=0.319, located in the blue-green region (point 1 in Fig. 10).

Fig. 8 shows the RT excitation (λ_{em}=543 nm fig. 8a) and emission (λ_{ex}=283 nm, fig. 8b) spectra of YF_3:3 mol% Tb^{3+} microstructures. The excitation spectrum is composed of some weak lines ascribed to spin-forbidden $4f^8$ to $4f^75d^1$ transition of Tb^{3+} (250–300 nm) and the f–f transitions of Tb^{3+} ion (300–500 nm) [24], the most intense band centered at 283 nm.

The emission spectrum of the YF_3:3 mol% Tb^{3+} microstructures under an excitation wavelength of 283 nm at room temperature is displayed in Fig. 8b. The fluorescence intensity of YF_3:3 mol% Tb^{3+} was unexpectedly high, emitting bright-green light. Successful doping with Tb^{3+} was evidenced from the splitting and the intensity pattern

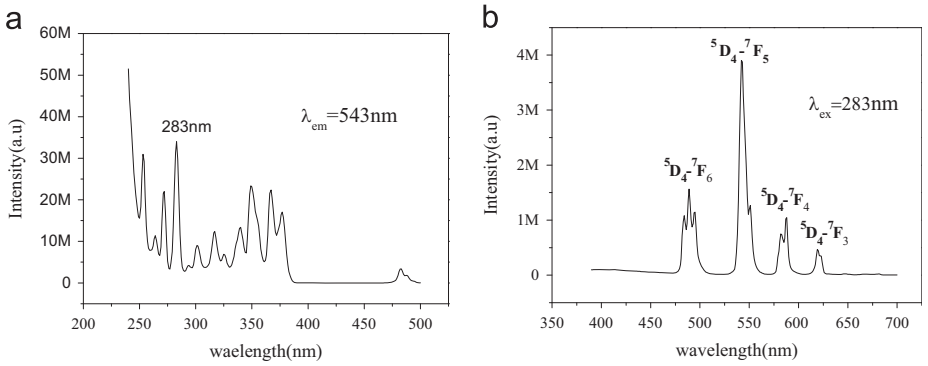

Fig. 8. RT photoluminescence spectra of YF_3:3 mol% Tb^{3+} truncated octahedra micro-/nanocrystal (EX slits=2 nm, EM slits=5 nm): (a) excitation spectra (λ_{em}=543 nm) and (b) emission spectra (λ_{ex}=283 nm).

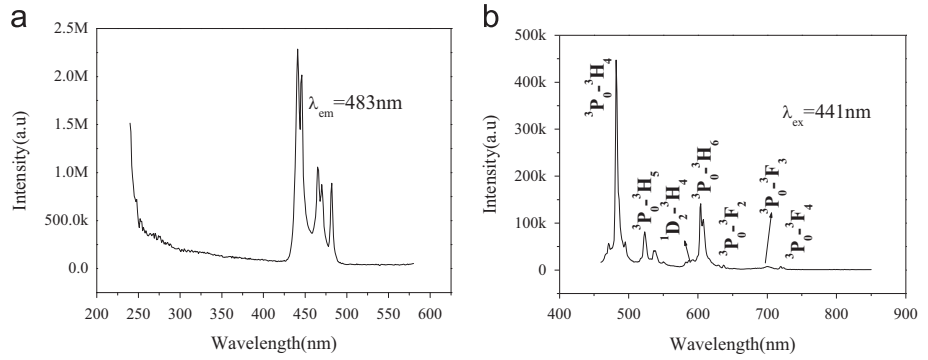

Fig. 9. RT photoluminescence spectra of YF_3: 0.3 mol% Pr^{3+} truncated octahedra micro-/nanocrystal (EX slits=2 nm, EM slits=5 nm): (a) excitation (λ_{em}= 604 nm) and (b) emission (λ_{ex}=441 nm).

of the luminescence lines. The emission spectrum exhibits four well-resolved peaks, centered at 489, 542, 588 and 619 nm, which have been observed for Tb-doped fluoride, corresponding to Tb electronic transmission of Tb^{3+} of $^5D_4$ to ^7F_J (J=6–3) [2,5,20]. Among them, the bright-green emission at 542 nm originating from $^5D_4$ to $^7F_5$ is the strongest. The CIE coordinates for the emission spectrum of YF_3:3 mol% Tb^{3+} are determined as x=0.297, y=0.534, located in the green region (point 2 in Fig. 10).

Fig. 9a shows the excitation spectrum of the 0.3 mol% Pr^{3+} doped YF_3 at room temperature, monitoring emission at 483 nm ($^3P_0$–$^3H_4$). Three excitation bands at 447 nm ($^3H_4$–$^3P_2$), 468 nm ($^3H_4$–$^3P_1$, $^1I_6$), and 482 nm ($^3H_4$–$^3P_0$) are observed from this spectrum. Comparing with the conventional Pr^{3+}-doped oxide phosphors [38], no obvious 4f–5d transition band of Pr^{3+} ions or host absorption band could be detected in the excitation spectrum. Due to the high electronegativity of pure fluoride systems, the threshold of the charge-transfer (CT) absorption is raised to a higher energy into the vacuum ultraviolet (VUV) region. When $\lambda < 250$ nm, there should have been a 4f–5d transition band of Pr^{3+} ions or host absorption band. Stefan et al. have reported that the excitation peaks of the lowest energetic 4f5d band are located at 183 nm and 204 nm [6]. We selected the 441 nm wavelength to measure the emission spectrum of Pr^{3+}-doped YF_3. Fig. 9b presents the emission spectrum of Pr^{3+} ions with a 441 nm excitation wavelength. Some distinct emission bands centered around 482, 523, 604, 637, and 720 nm which were assigned to the $^3P_0$–^3H_J (J=4, 5, and 6), and $^3P_0$–^3F_J (J=2, 3, and 4) transitions [20] are observed from this spectrum. Additionally, a very weak peak was observed around 588 nm, corresponding to the $^1D_2$-$^3H_4$ transition. Due to the large energy gap between $^3P_0$ and $^1D_2$ and the low phonon energy [39], multiphonon nonradiative relaxation from $^3P_0$ to $^1D_2$ is very small, and hence the $^1D_2$ luminescence was more difficult to observe. Pr^{3+} will show blue upconversion both of ESA (two photon) and ETU (three photon) types from $^3P_0$ state when pumping into the $^1D_2$ state. The CIE coordinates for the emission spectrum of YF_3:0.3 mol% Pr^{3+} are determined as x=0.308, y=0.362, located in the green region (point 3 in Fig. 10).

4. Conclusion

In summary, high quality YF_3:Ln^{3+} nano-/microcrystals have been synthesized using a simple hydrothermal approach. The morphological evolution process was observed by time-dependent reaction. The possible growth mechanisms are proposed. The as-obtained hexagonal YF_3:Ln^{3+} (Ln=Sm, Pr, Tb and Dy) nano-/microcrystals show strong light emissions with different colors coming from different activator ions under room temperature. The morphology and size of the products have great influence on their emission intensity. Additionally, we observed the

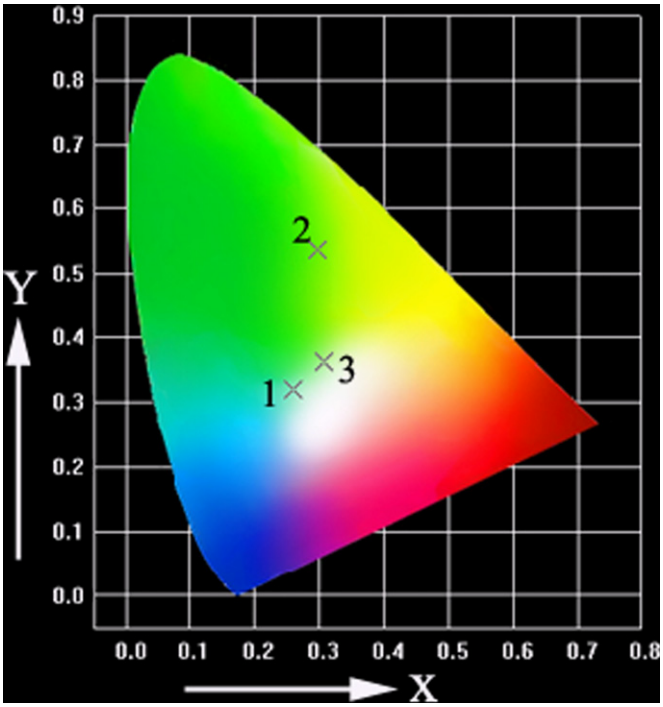

Fig. 10. CIE chromaticity diagram showing the emission colors for (1) YF_3:3 mol% Dy^{3+}; (2) YF_3:3 mol% Tb^{3+}; (3) YF_3:0.3 mol% Pr^{3+} truncated octahedra micro-/nanocrystal. (For interpretation of the references to color in this figure legend, the reader is referred to the web version of this article.)

energy transition of Sm^{3+}–Sm^{2+} in PL spectra, which is quite different from those reported previously. The obtained nano-/microcrystals might have potential applications in light phosphor powders and advanced flat panel display devices.

Acknowledgments

This work was supported by National Natural Science Foundation of China (61174012), Science and Technological Fund of Anhui Province for Outstanding Youth (08040106824), Foundation for Excellent Talents in University by Anhui Province (2012SQRL082ZD) and Youth Fund of Anhui Polytechnic University (2008yq028zd).

References

[1] K. Binnemans, Lanthanide-based luminescent hybrid materials, Chemical Reviews 109 (2009) 4283–4374.
[2] Q.Y. Zhang, X.Y. Huang, Recent progress in quantum cutting phosphors, Progress in Materials Science 55 (2010) 353–427.
[3] C.S. Yoo, H.B. Radousky, N.C. Holmes, N.M. Edelstein, Luminescence of Sm^{2+} ions as a probe of pressure-induced phase transitions in SrF_2, Physical Review B 44 (1991) 830–833.
[4] J.J. Li, R.F. Wei, X.Y. Liu, H. Guo, Enhanced luminescence via energy transfer from Ag^{+} to RE ions (Dy^{3+}, Sm^{3+}, Tb^{3+}) in glasses, Optics Express 20 (2012) 10122–10127.
[5] J. Kuang, Y. Liu, J. Zhang, White-light-emitting long-lasting phosphorescence in Dy^{3+}-doped $SrSiO_3$, Journal of Solid State Chemistry 179 (2006) 266–269.
[6] L.X. Yu, H.W. Song, Z.X. Liu, L.M. Yang, S.Z. Lu, Z.H. Zheng, Electronic transition and energy transfer processes in $LaPO_4$-Ce^{3+}/Tb^{3+} nanowires, Journal of Physical Chemistry B 109 (2005) 11450–11455.
[7] S. kück, I. Sokolska, Spectroscopic investigation of Mn^{2+}, Pr^{3+} codoped $KMgF_3$ under vacuum-ultraviolet excitation, Journal of Physics: Condensed Matter 18 (2006) 5447–5457.
[8] A. Braud, S. Girard, J.L. Doualan, M. Thuau, R. Moncorge, A.M. Tkachuk, Energy-transfer processes in Yb:Tm-doped KY_3F_{10}, $LiYF_4$, and BaY_2F_8 single crystals for laser operation at 1.5 and 2.3 μm, Physical Review B 61 (2000) 5280–5292.
[9] F. Wang, Y. Han, C.S. Lim, Y.H. Lu, J. Wang, J. Xu, H.Y. Chen, C. Zhang, M.H. Hong, X.G. Liu, Simultaneous phase and size control of upconversion nanocrystals through lanthanide doping, Nature 463 (2010) 1061–1065.
[10] A. Baszczuk, M. Jasiorski, M. Nyk, J. Hanuza, M. Maczka, W. Atrek, Luminescence properties of europium activated $SrIn_2O_4$, Journal of Alloys and Compounds 394 (2005) 88–94.
[11] T. Matsuzawa, Y. Aoki, N. Takeuchi, Y. Murayama, A new long phosphorescent phosphor with high brightness, $SrAl_2O_4$:Eu^{2+}, Dy^{3+}, Journal of the Electrochemical Society 143 (1996) 2670–2673.
[12] X. Liu, J. Lin, Synthesis and luminescent properties of $LaInO_3$:RE^{3+} (RE=Sm, Pr and Tb) nanocrystalline phosphors for field emission displays, Solid State Sciences 11 (2009) 2030–2036.
[13] X. Wang, J. Zhuang, Q. Peng, Y.D. Li, A general strategy for nanocrystal synthesis, Nature 437 (2005) 121–124.
[14] J.L. Lemyre, A.M. Ritcey, Synthesis of lanthanide fluoride nanoparticles of varying shape and size, Chemistry of Materials 17 (2005) 3040–3043.
[15] L.W. Qian, J.T. Zai, Z. Chen, J. Zhu, Y.P. Yuan, X.F. Qian, Control of the morphology and composition of yttrium fluoride *via* a salt-assisted hydrothermal method, CrystEngComm 12 (2010) 199–206.
[16] S. Wang, S.Y. Song, R.P. Deng, H.L. Guo, Y.Q. Lei, F. Cao, X.Y. Li, S.Q. Su, H.J. Zhang, Hydrothermal synthesis and upconversion photoluminescence properties of lanthanide doped YF_3 submicroflowers, CrystEngComm 12 (2010) 3537–3541.
[17] G.Y. Li, Y.H. Ni, J.M. Hong, K.M. Liao, Controllable synthesis of polyhedral YF_3 microcrystals *via* a potassium sodium tartrate-assisted hydrothermal route, CrystEngComm 10 (2008) 1681–1686.
[18] N.O. Nuñez, H. Míguez, M. Quintanilla, E. Cantelar, F. Cussó, M. Ocaña, Uniform Yb,Er:YF_3 up-conversion nanophosphors of various morphologies synthesised in polyol media through an ionic liquid, Journal of Nanoparticle Research 12 (2010) 2553–2565.
[19] L.Y. Wang, Y. Zhang, Y.Y. Zhu, One-pot synthesis and strong near-infrared upconversion luminescence of poly (acrylic acid)-functionalized YF_3:Yb^{3+}/Er^{3+} nanocrystals, Nano Research 3 (2010) 317–325.
[20] C. Peng, C. Li, G. Li, S. Li, J. Lin, YF_3:Ln^{3+} (Ln=Ce, Tb, Pr) submicrospindles: hydrothermal synthesis and luminescence properties, Dalton Transactions 41 (2012) 8660–8668.
[21] F. Pellé, M. Dhaouadi, L. Michely, P. Aschehoug, A. Toncelli, S. Veronesi, M. Tonelli, Spectroscopic properties and upconversion in Pr^{3+}:YF_3 nanoparticles, Physical Chemistry Chemical Physics 13 (2011) 17453–17460.
[22] F.N. Sayed, V. Grover, S.V. Godbole, A.K. Tyagi, Color tunable YF_3: Ce^{3+}/Ln^{3+} (Ln^{3+}: Eu^{3+}, Tb^{3+}, Dy^{3+}, Sm^{3+}) luminescent system: role of sensitizer and energy transfer study, RSC Advances 2 (2012) 1161–1167.
[23] L. Aarts, B. van der Ende, M.F. Reid, A. Meijerink, Downconversion for solar cells in YF_3:Pr^{3+}, Yb^3, Spectroscopy Letters 43 (2010) 373–381.
[24] G. Jia, H.P. You, M. Yang, L.H. Zhang, H.J. Zhang, Uniform lanthanide orthoborates $LnBO_3$ (Ln=Gd, Nd, Sm, Eu, Tb, and Dy) microplates: general synthesis and luminescence properties, Journal of Physical Chemistry C 113 (2009) 16638–16644.
[25] F. Tao, Z.J. Wang, L.Z. Yao, W.L. Cai, X.G. Li, Synthesis and photoluminescence properties of truncated octahedral Eu-doped YF_3 submicrocrystals or nanocrystals, Journal of Physical Chemistry C 111 (2007) 3241–3245.

[26] Z. Fang, Q. Wang, X. Wang, B. Zhu, F. Fan, C. Wang, X. Liu, Ethylenediamine inducing growth of {100} facets exposed PbS nanosheets, Crystal Research and Technology 47 (2012) 635–642.
[27] G.M. Whitesides, B. Graybowski, Self-Assembly at All Scales, Science 295 (2002) 2418–2421.
[28] Y. Chang, H.C. Zeng, Manipulative synthesis of multipod frameworks for self-organization and self-amplification of Cu_2O microcrystals, Crystal Growth Design 4 (2004) 273–278.
[29] H.G. Yang, H.C. Zeng, Self-construction of hollow SnO_2 octahedra based on two-dimensional aggregation of nanocrystallites, Angewandte Chemie International Edition 43 (2004) 5930–5933.
[30] F. Tao, F. Pan, Z.J. Wang, W.L. Cai, L.Z. Yao, Synthesis and photoluminescence properties of hexagonal Lanthanide(III)-doped $NaYF_4$ microprisms, ChemEngComm 12 (2010) 4263–4267.
[31] J. Rubio O., Doubly-valent rare-earth ions in halide crystals, Journal of Physics and Chemistry of Solids 52 (1991) 101–174.
[32] P.S. Peijzel, Probing High Energy Levels of Lanthanide Ions: Experiment and Theory, Utrecht University, Netherlands, 2004.
[33] W. Kaiser, C.G.B. Garrett, D.L. Wood, Fluorescence and optical maser effects in CaF_2:Sm^{++}, Physical Review 123 (1961) 766–776.
[34] D.L. Wood, W. Kaiser, Absorption and fluorescence of Sm^{2+} in CaF_2, SrF_2, and BaF_2, Physical Review 126 (1962) 2079–2088.
[35] R. Stefania, A.D. Maiaa, E.E.S. Teotonioa, M.A.F. Monteiroa, M.C.F.C. Felintob, H.F. Britoa, Photoluminescent behavior of SrB_4O_7:RE^{2+} (RE=Sm and Eu) prepared by Pechini, combustion and ceramic methods, Journal of Solid State Chemistry 179 (2006) 1086–1092.
[36] A.N. Georgobiani, B.G. Tagiev, O.B. Tagie, K.B. Ganbarova, Photoluminescence of Ga_2S_3:Sm^{2+} crystals, Inorganic Materials 44 (2008) 563–565.
[37] H. Choi, Ch.H. Kim, C.H. Pyun, S.J. Kim, Luminescence of (Ca, La)S: Dy, Journal of Luminescence 82 (1999) 25–32.
[38] P. Dorenbos, The $4f^n \leftrightarrow 4f^{n-1}5d$ transitions of the trivalent lanthanides in halogenides and chalcogenides, Journal of Luminescence 91 (2000) 91–106.
[39] Y. Chen, F. Auzel, Investigation of multiphonon assisted side band absorptions in rare-earth-doped halide glasses and crystals, Journal of Non-Crystalline Solids 184 (1995) 278–281.